



# Enhanced formaldehyde oxidation on CeO<sub>2</sub>/AlOOH-supported Pt catalyst at room temperature



Zhaoxiong Yan <sup>a,b</sup>, Zhihua Xu <sup>a,b</sup>, Jiaguo Yu <sup>a,d,\*\*</sup>, Mietek Jaroniec <sup>c,\*</sup>

<sup>a</sup> State Key Laboratory of Advanced Technology for Materials Synthesis and Processing, Wuhan University of Technology, Wuhan 430070, PR China

<sup>b</sup> Hubei Key Laboratory for Processing and Application of Catalytic Materials, Huanggang Normal University, Huanggang 438000, PR China

<sup>c</sup> Department of Chemistry and Biochemistry, Kent State University, Kent, OH 44242, USA

<sup>d</sup> Department of Physics, Faculty of Science, King Abdulaziz University, Jeddah 21589, Saudi Arabia

## ARTICLE INFO

### Article history:

Received 23 February 2016

Received in revised form 25 May 2016

Accepted 21 June 2016

Available online 22 June 2016

### Keywords:

Catalytic oxidation

Adsorption

Formaldehyde removal

Nanostructured catalyst

## ABSTRACT

A CeO<sub>2</sub>/AlOOH-supported Pt catalyst was prepared by combining the microemulsion-assisted synthesis of AlOOH and CeO<sub>2</sub> hybrid with NaBH<sub>4</sub>-reduction of Pt precursor. The as-prepared catalyst obtained by depositing Pt nanoparticles on the CeO<sub>2</sub>/AlOOH (1:9 molar ratio) support (Pt/Al<sub>9</sub>Ce<sub>1</sub>) exhibited a remarkable catalytic activity and stability for oxidative removal of formaldehyde (HCHO) vapor at room temperature. The excellent performance of Pt/Al<sub>9</sub>Ce<sub>1</sub> catalyst could be attributed to the abundance of surface hydroxyls, oxygen storage in CeO<sub>2</sub>, high dispersion of Pt nanoparticles, and excellent adsorption performance of AlOOH. The mechanism of HCHO decomposition was investigated with respect to the behavior of adsorbed intermediates on the Pt/Al<sub>9</sub>Ce<sub>1</sub> surface at room temperature using *in situ* DRIFTS. The results suggest that the main species formed on the surface during HCHO oxidation are the reaction intermediates, which could be directly oxidized to CO<sub>2</sub> in the presence of O<sub>2</sub>. By taking advantage of high adsorption affinity of AlOOH nanoflakes toward HCHO, reducible ceria nanoparticles and excellent catalytic activity of Pt nanoparticles toward HCHO oxidation, it was possible to design a superior nanostructured catalyst for room temperature decomposition of HCHO. This strategy can be also applied to fabricate novel nanostructured catalysts for advanced applications such as environmental remediation.

© 2016 Elsevier B.V. All rights reserved.

## 1. Introduction

Formaldehyde (HCHO) is one of the major pollutants of indoor air, which is usually released from composite and laminated wood-based building products, textiles, carpeting, adhesives and electronic equipment. HCHO can impose serious health disorders on human beings such as eye irritation, breathing difficulty and even nasal cancer [1,2]. Therefore, the elimination of HCHO is of practical interest at ambient temperatures. Various methods including adsorption [3–5], photocatalysis [6–8] and catalytic oxidation [9–13] have been investigated to abate HCHO in indoor environment. Among them, catalytic oxidation is considered as a promising method because it leads to a complete decomposition of HCHO into CO<sub>2</sub> and H<sub>2</sub>O. Therefore, there is a great interest in the development of effective catalysts for catalytic oxidation

of HCHO at ambient temperatures. So far, the transition-metal oxides like Co<sub>3</sub>O<sub>4</sub> and MnO<sub>2</sub> [14–16], and rare earth oxides such as CeO<sub>2</sub>, LaCoO<sub>3</sub> and LaMnO<sub>3</sub> [10,17] have been investigated for catalytic oxidation of HCHO. However, their catalytic activity towards HCHO oxidation is usually at temperatures above 40 °C, and their performance is inadequate for potential applications. Taking into account the environmental friendliness and energy-saving aspects, the supported noble-metal catalysts are believed to be effective for complete oxidation of HCHO especially at room temperature [18–22]. A variety of materials including TiO<sub>2</sub> [23–29], CeO<sub>2</sub> [30], Al<sub>2</sub>O<sub>3</sub> [31], FeO<sub>x</sub> [20], ferrihydrite [32] and SiO<sub>2</sub> [33] were explored as the potential supports of noble metals for room-temperature removal of HCHO. Recently, we found that the Pt supported on AlOOH nanoflakes (Pt/AlOOH) showed higher catalytic activity toward decomposition of HCHO at room temperature as compared to the Pt supported on commercial Al<sub>2</sub>O<sub>3</sub> and Pt on P25 [34]. The high activity of the Pt/AlOOH catalyst was attributed to the abundance of surface hydroxyls, high dispersion of Pt nanoparticles, excellent adsorption performance of AlOOH, and the high specific surface area and large pore volume of the catalyst. Generally, it is recognized that the catalytic activity of a supported noble-metal

\* Corresponding author.

\*\* Corresponding author at: State Key Laboratory of Advanced Technology for Materials Synthesis and Processing, Wuhan University of Technology, Wuhan 430070, PR China.

E-mail addresses: [jiaguoyu@yahoo.com](mailto:jiaguoyu@yahoo.com) (J. Yu), [jaroniec@kent.edu](mailto:jaroniec@kent.edu) (M. Jaroniec).

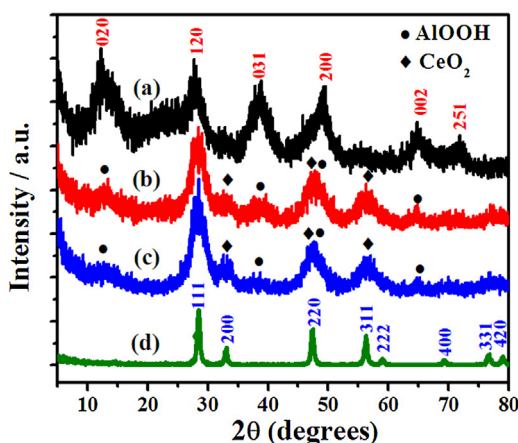


**Fig. 1.** XRD patterns of (a) Pt/Al, (b) Pt/Al<sub>9</sub>Ce<sub>1</sub>, (c) Pt/Al<sub>7</sub>Ce<sub>3</sub> and (d) Pt/Ce.

catalyst is closely correlated to its microstructure, composition, surface hydroxyls, surface valence states of both the support and noble metal, and the support type. In spite of significant advances in the development of supported catalysts, many issues are still not fully explained such as the interaction between active sites and the support surface.

Ceria (CeO<sub>2</sub>) has been extensively investigated in heterogeneous catalysis, such as water-gas shift [35,36], CO oxidation [37,38], methanol-steam reforming and biofuel production [39,40], and HCHO oxidation [41] due to its redox properties associated with facile conversion of Ce<sup>4+</sup> to Ce<sup>3+</sup>. Recently, the nanometer-sized ceria-containing hybrid materials with a variety of applications as adsorbents, catalysts and electrode materials [42–46] have attracted a lot of attention due to the intimate interactions between supports and ceria nanoparticles that may potentially induce electronic perturbations at the interface leading to the catalytic performance, which is unachievable in the case of bulk ceria. CeO<sub>2</sub> and AlOOH nanocomposite seems to be an interesting support for noble metal catalysts towards room temperature HCHO oxidation due to the great affinity of AlOOH for HCHO and remarkable oxygen storage ability of CeO<sub>2</sub> [41]. Herein, we report Pt nanoparticles supported on a porous AlOOH and CeO<sub>2</sub> nanocomposite prepared by microemulsion-assisted process for HCHO oxidation at room temperature. It is expected that the incorporation of CeO<sub>2</sub> into AlOOH may enhance the catalytic activity of Pt/AlOOH due to the synergistic effect between CeO<sub>2</sub>, AlOOH and Pt nanoparticles, which could generate more active oxygen species and accelerate the oxidation of HCHO molecules, and eventually improve the catalytic performance.

## 2. Experimental section

### 2.1. Synthesis of the supports and catalysts

In a typical synthesis, a mixture containing 100 mL of cyclohexane and 20.5 g of polyethylene glycol (PEG 400) was magnetically stirred and heated to 70 °C. 20 mL of the mixed solution of Al(NO<sub>3</sub>)<sub>3</sub>·9H<sub>2</sub>O (0.009 mol) and Ce(NO<sub>3</sub>)<sub>4</sub>·6H<sub>2</sub>O (0.001 mol) were added to the above mixture. After stirring for 10 min, 3.50 g of NH<sub>3</sub> solution (27 wt%) was added stepwise, and aged for 2 h at 70 °C. The mixture was separated by centrifugation, and the hydrogel was washed with deionized water and ethanol for five times, respectively. Finally, the hydrogel was dried at 80 °C overnight and the resulting support was denoted as Al<sub>9</sub>Ce<sub>1</sub>.

The other syntheses of supports were performed analogously, but the different solutions were used such as Al(NO<sub>3</sub>)<sub>3</sub>·9H<sub>2</sub>O (0.007 mol) and Ce(NO<sub>3</sub>)<sub>4</sub>·6H<sub>2</sub>O (0.003 mol) or

Ce(NO<sub>3</sub>)<sub>4</sub>·6H<sub>2</sub>O (0.01 mol) or Al(NO<sub>3</sub>)<sub>3</sub>·9H<sub>2</sub>O (0.01 mol) instead of Al(NO<sub>3</sub>)<sub>3</sub>·9H<sub>2</sub>O (0.009 mol) and Ce(NO<sub>3</sub>)<sub>4</sub>·6H<sub>2</sub>O (0.001 mol) to obtain the following supports Al<sub>7</sub>Ce<sub>3</sub>, CeO<sub>2</sub> and AlOOH, respectively.

The Al<sub>9</sub>Ce<sub>1</sub>-supported Pt catalyst was obtained by adding 0.4 g of the as-prepared Al<sub>9</sub>Ce<sub>1</sub> into 30 mL of deionized water, then the specified amount of H<sub>2</sub>PtCl<sub>6</sub> solution was added under magnetic stirring to achieve the nominal weight of Pt equal to 0.8 wt%. After impregnation for 20 min, 5 mL of the mixed solution of NaBH<sub>4</sub> (0.1 mol/L) and NaOH (0.1 mol/L) was quickly added into the suspension under vigorous stirring for 30 min, and the resulting powder was washed twice with deionized water and twice with ethanol. The sample was dried at 80 °C overnight and denoted as Pt/Al<sub>9</sub>Ce<sub>1</sub>. For the purpose of comparison, the same nominal weight of Pt was deposited over Al<sub>7</sub>Ce<sub>3</sub> (denoted as Pt/Al<sub>7</sub>Ce<sub>3</sub>), CeO<sub>2</sub> (denoted as Pt/Ce), AlOOH (denoted as Pt/Al), commercial Al<sub>2</sub>O<sub>3</sub> (Pt/c-Al<sub>2</sub>O<sub>3</sub>) and over P25 (Pt/TiO<sub>2</sub>).

### 2.2. Characterization

X-ray diffraction (XRD) patterns of the samples were obtained using a Philips X'Pert powder X-ray diffractometer with Cu K $\alpha$  radiation ( $\lambda = 0.15419$  nm). The morphology of the samples was characterized on a JEM-2100F transmission electron microscope (TEM) (JEOL, Japan). The actual chemical compositions of the as-prepared samples were measured by inductively coupled plasma atomic emission spectrometry (ICP-AES) using an Optima 4300 DV spectrometer (PerkinElmer). Nitrogen adsorption-desorption isotherms were obtained on an ASAP 2020 (Micromeritics Instruments, USA). All samples were degassed at 100 °C prior to adsorption measurements. The Brunauer–Emmett–Teller (BET) surface area ( $S_{\text{BET}}$ ) was determined by a multipoint BET method using adsorption data in the relative pressure  $P/P_0$  range of 0.05–0.2. The single-point pore volume ( $V_p$ ) was estimated from the amount adsorbed at a relative pressure of 0.98. The pore size distributions (PSD) were calculated using adsorption branches of nitrogen adsorption-desorption isotherms. X-ray photoelectron spectroscopy (XPS) data were obtained using an ESCALAB250xi spectrometer (Thermo Scientific). All the binding energies were referenced to the C1s peak at 284.8 eV of the surface adventitious carbon. Measurements of the metal dispersion and hydrogen temperature-programmed reduction (H<sub>2</sub>-TPR) were carried out on the BELCAT-B (Japan) instrument at room temperature. For metal dispersion measurements, the samples were first reduced under pure hydrogen (50 mL min<sup>-1</sup>) at 200 °C for 1 h and further outgassed under He (50 mL min<sup>-1</sup>) for 0.5 h at the same temperature. Subsequently, CO pluses were injected into the carrier gas intermittently after the sample was cooled to room temperature, and the whole process was monitored by TCD. For H<sub>2</sub>-TPR experiments, the samples were pretreated in He (50 mL min<sup>-1</sup>) at 120 °C for 1 h and then the temperature was ramped from room temperature to 450 °C at 10 °C min<sup>-1</sup> with the introduction of the reducing gas (10% H<sub>2</sub>/Ar) at a flow rate of 30 mL min<sup>-1</sup>.

In-situ diffused Fourier transform infrared spectroscopy (DRIFTS) patterns were recorded on Thermo Fisher 6700 instrument. The catalysts were pretreated in a dry air flow at 150 °C for 1 h in an in-situ cell reactor. Then the reactant gas mixture (78 ppm HCHO + O<sub>2</sub>) was introduced into the DRIFT cell at room temperature via separate mass flow meters at flow rates of 30 mL min<sup>-1</sup>. All spectra were recorded with a resolution of 4 cm<sup>-1</sup>, and the background spectrum was subtracted from each spectrum, respectively.

### 2.3. HCHO removal measurements

The HCHO removal tests were performed at room temperature in an organic glass box covered by a layer of aluminum foil

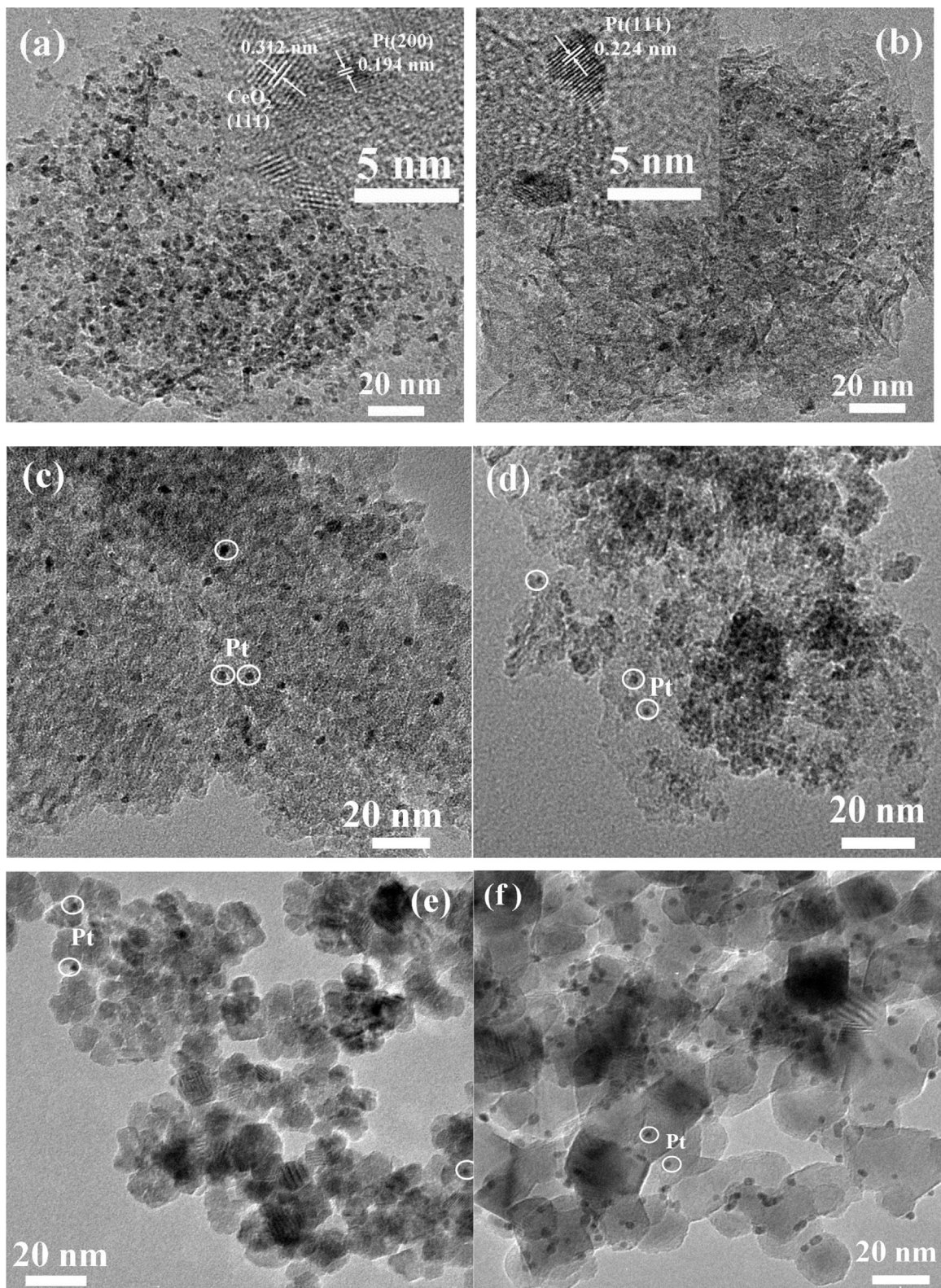


**Fig. 2.** TEM and HRTEM (inset) images of (a) Pt/Al<sub>9</sub>Ce<sub>1</sub>, (b) Pt/Al, (c) Pt/c-Al<sub>2</sub>O<sub>3</sub>, (d) Pt/Al<sub>7</sub>Ce<sub>3</sub>, (e) Pt/Ce and (f) Pt/TiO<sub>2</sub>.

on its inner wall. 0.1 g of the as-prepared sample was dispersed on the bottom of a glass petri dish having a diameter of 14 cm. After placing the sample-contained dish in the bottom of reactor with a glass slide cover, a certain amount of condensed HCHO (38%) was injected into the reactor with a 5 W fan in the bottom of reactor. After 2–3 h, the HCHO solution was volatilized com-

pletely and the concentration of HCHO was stabilized. HCHO, CO<sub>2</sub>, CO and water vapor was on-line analyzed with a Photoacoustic IR Multigas Monitor (INNOVA air Tech Instruments Model 1412). The HCHO vapor was allowed to reach adsorption/desorption equilibrium within the reactor prior to the experiment. The glass slide cover on the petri dish was removed to start adsorption or cat-

alytic oxidation reaction of HCHO, when the initial concentration of HCHO after adsorption/desorption equilibrium remained constant. During the catalytic oxidation reaction, carbon dioxide concentration increased and the HCHO concentration decreased steadily with time. The  $\Delta\text{CO}_2$  concentration increase (ppm,  $\Delta\text{CO}_2$ , which is the difference between  $\text{CO}_2$  concentration at a reaction time  $t$  and initial  $\text{CO}_2$  concentration) and the HCHO concentration decrease were used to evaluate the adsorption and catalytic performance.

### 3. Results and discussion

**Fig. 1** shows the wide-angle XRD patterns of Pt/Al, Pt/ $\text{Al}_9\text{Ce}_1$ , Pt/ $\text{Al}_7\text{Ce}_3$  and Pt/Ce. All the diffraction peaks on the XRD pattern of Pt/Al can be related to  $\gamma$ -AlOOH (JCPDS No. 21-1307), and their intensities are weak, indicating poor crystallinity and/or small size of crystallites of  $\gamma$ -AlOOH. The pattern of Pt/Ce shows a distinct crystal phase of fluorite oxide-type  $\text{CeO}_2$  (JCPDS No. 43-1002). For Pt/ $\text{Al}_9\text{Ce}_1$  and Pt/ $\text{Al}_7\text{Ce}_3$  catalysts, mixed phases of AlOOH and  $\text{CeO}_2$  are observed; the diffraction intensities of  $\text{CeO}_2$  decrease, whereas those of AlOOH increase with the Al/Ce atomic ratio increasing from 7:3 to 9:1. This behavior implies that as expected the Pt/ $\text{Al}_9\text{Ce}_1$  catalyst contained a larger amount of AlOOH than Pt/ $\text{Al}_7\text{Ce}_3$ . The characteristic peaks of Pt (the most strongest peak at 39.8°) are not observed in all catalysts mainly due to the low loading of Pt, small particle size and high dispersion of Pt on the supports [47].

The TEM and HRTEM images of Pt/ $\text{Al}_9\text{Ce}_1$  and Pt/Al are shown in **Fig. 2**. In both cases the AlOOH supports are in the form of agglomerated ultra-thin nanoflakes. In the case of the Pt/ $\text{Al}_9\text{Ce}_1$  catalyst,  $\text{CeO}_2$  nanoparticles are dispersed on the AlOOH nanoflakes, and their particle size is ca. 3–5 nm. The fringes of the  $\text{CeO}_2$  crystal lattice are clear and the distance between two adjacent lattice planes is ca. 0.312 nm (see inset in **Fig. 2a**), which is consistent with the d-value of the (111) lattice planes of  $\text{CeO}_2$  [41], further suggesting the presence of  $\text{CeO}_2$  in the Pt/ $\text{Al}_9\text{Ce}_1$  catalyst. Pt nanoparticles are also very small in size (ca. 2–3 nm), and the interplanar spacing is ca. 0.194 nm corresponding to the (200) plane for metallic Pt [48,49]. Moreover, the boundary between Pt and  $\text{CeO}_2$  nanoparticles is not distinctly clear, indicating a strong interaction between Pt and  $\text{CeO}_2$  nanoparticles [41]. The interaction between Pt and  $\text{CeO}_2$  is important, which contribute to the weakening the Ce–O bond and thus enhance the activity of the catalyst [21]. For Pt/Al catalyst, Pt nanoparticles (dark dots) are observed on the AlOOH support, and the interplanar spacing plane is ca. 0.224 nm corresponding to the (111) plane of metallic Pt [48,49]. The Pt nanoparticles on Pt/ $\text{Al}_7\text{Ce}_3$ , Pt/Ce, Pt/TiO<sub>2</sub> and Pt/c-Al<sub>2</sub>O<sub>3</sub> catalysts are also in the range of 2–5 nm. This result indicates that Pt nanoparticles are successfully deposited on the supports. The ICP analysis showed that the percentages of Pt, Al, Ce and Na in Pt/ $\text{Al}_9\text{Ce}_1$  are 0.9%, 24.4%, 7.9% and 0.5%, respectively; while the percentages of Pt, Al and Na in Pt/Al are 1.0%, 31.2% and 0.2%, respectively. As shown in [29] the presence of Na<sup>+</sup> was beneficial for the room temperature oxidation of HCHO as evidenced by higher oxidation activity of the catalysts [29]. In addition, the measured Pt dispersion on the Pt/ $\text{Al}_9\text{Ce}_1$  catalyst is ca. 21.6%, similar to that on the Pt/Al catalyst (21.9%). This implies that the addition of  $\text{CeO}_2$  does not affect much the dispersion of noble metals on the support surface.

**Fig. 3** shows the N<sub>2</sub> adsorption-desorption isotherms and the corresponding pore-size distribution curves (inset) for Pt/ $\text{Al}_9\text{Ce}_1$  and Pt/Al. The BET specific surface area ( $S_{\text{BET}}$ ), pore volume ( $V_p$ ) and pore width ( $d_p$ ) at the maximum of PSD for the samples studied are listed in **Table 1**. Adsorption isotherms are type IV with H<sub>2</sub> hysteresis loop, indicating the presence of interconnected mesopores with some constrictions [50]. The pore-size distribution curves (inset in **Fig. 3**) of Pt/ $\text{Al}_9\text{Ce}_1$  and Pt/Al are bimodal with small mesopores (peaks at ca. 3.0 and 2.6 nm for Pt/ $\text{Al}_9\text{Ce}_1$  and Pt/Al,

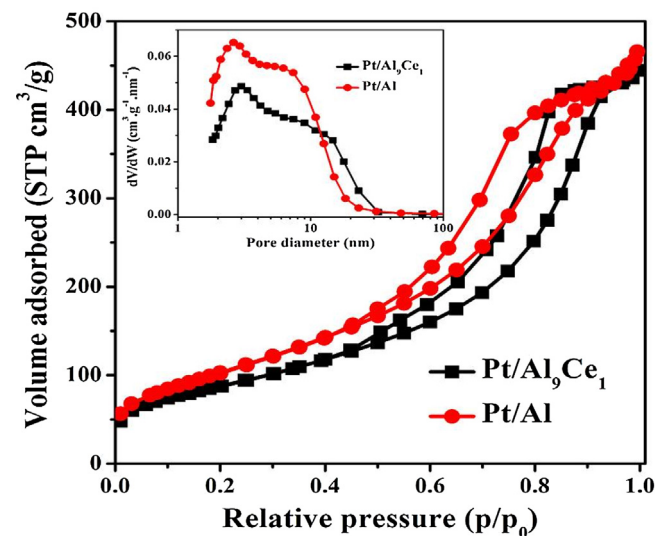


**Fig. 3.** Nitrogen adsorption/desorption isotherms and the corresponding pore size distributions (inset) obtained for Pt/ $\text{Al}_9\text{Ce}_1$  and Pt/Al.

**Table 1**  
Properties of the supports and catalysts studied.

Sample	$S_{\text{BET}}$ (m <sup>2</sup> /g)	$d_p$ (nm)	$V_p$ (cm <sup>3</sup> /g)
Pt/Al	359	2.6, 6.2	0.68
Pt/ $\text{Al}_9\text{Ce}_1$	318	3.0, 9.0	0.67
Pt/ $\text{Al}_7\text{Ce}_3$	244	2.0, 12.7	0.54
Pt/Ce	59	2.0, 12.3	0.19
AlOOH	396	2.9, 6.2	0.73
$\text{Al}_9\text{Ce}_1$	333	2.6, 12.5	0.88
$\text{CeO}_2$	69	2.1	0.24
Pt/TiO <sub>2</sub>	45	2.0	0.09
Pt/c-Al <sub>2</sub> O <sub>3</sub>	143	3.3	0.18

respectively) and larger mesopores (peaks at ca. 9.0 and 6.2 nm for Pt/ $\text{Al}_9\text{Ce}_1$  and Pt/Al, respectively), further confirming the mesoporosity of the catalysts. The smaller mesopores reflect the porosity in the nanoflakes, while the larger mesopores are related to the pores formed between the stacked nanoflakes and/or nanoparticles. Pt/ $\text{Al}_9\text{Ce}_1$  shows larger mesopores, smaller  $S_{\text{BET}}$  and similar  $V_p$  as compared to Pt/Al. The larger pores in Pt/ $\text{Al}_9\text{Ce}_1$  would facilitate the diffusion of HCHO into the interior of the catalyst.

The surface chemical composition and chemical state of Pt/ $\text{Al}_9\text{Ce}_1$  and Pt/Al catalysts were characterized by XPS. As shown in **Fig. 4a**, both the samples contain Al, O, and Pt elements. In addition, Ce peaks are observed on the spectrum of Pt/ $\text{Al}_9\text{Ce}_1$ , further indicating the deposition of  $\text{CeO}_2$  on the AlOOH support. The high resolution XPS spectra of Pt 4f and Al 2p regions for the Pt/ $\text{Al}_9\text{Ce}_1$  and Pt/Al samples are shown in **Fig. 4b**. Two peaks located at 70.8–70.9 and 74.2–74.3 eV are observed for both samples, which are assigned to Pt 4f<sub>7/2</sub> of metallic Pt [51] and Al 2p [52], respectively, implying that Pt NPs were successfully deposited on the supports.

As shown in **Fig. 4c**, the O 1s signal of Pt/ $\text{Al}_9\text{Ce}_1$  and Pt/Al could be deconvoluted into two peaks. The peaks at 530.4–530.5 and 532 eV are attributed to the lattice O ( $\text{O}_L$ ) and hydroxyl O and/or surface adsorbed O ions ( $\text{O}_{\text{II}}$ ), respectively [20,53]. Pt/ $\text{Al}_9\text{Ce}_1$  has a lower percentage of  $\text{O}_{\text{II}}$  as compared to Pt/Al (**Table 2**), presumably due to the smaller amount of AlOOH in Pt/ $\text{Al}_9\text{Ce}_1$ . The percentage of  $\text{O}_{\text{II}}$  in Pt/Al and Pt/ $\text{Al}_9\text{Ce}_1$  is much larger than that in the Pt/ $\text{Al}_7\text{Ce}_3$ , Pt/Ce, Pt/TiO<sub>2</sub> and Pt/c-Al<sub>2</sub>O<sub>3</sub> catalysts (listed in **Table 2**), which may lead to the difference in the activity of these catalysts toward oxidative decomposition of HCHO. The high resolution XPS spectrum of Ce 3d (**Fig. 4d**) can be deconvoluted into 882.6, 888.4, 898.0, 901.0, 907.4,

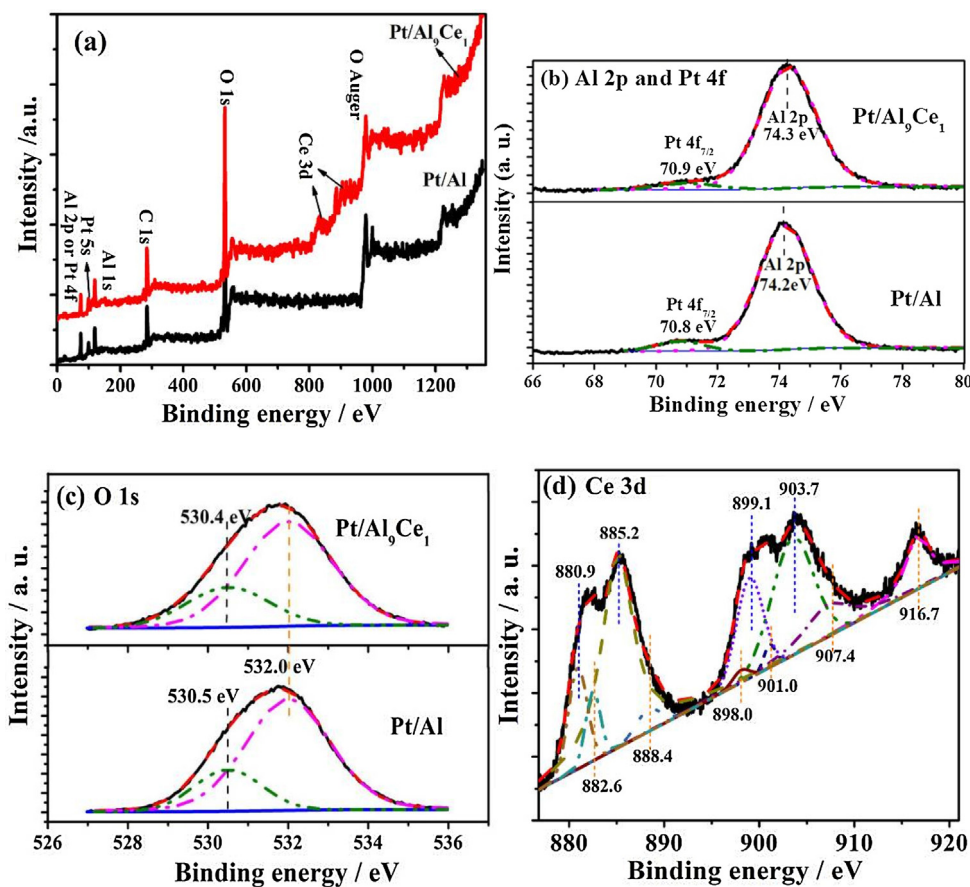


**Fig. 4.** XPS survey spectra (a) and high resolution XPS spectra for Al 2p and Pt 4f (b), and O 1s (c) of Pt/Al<sub>9</sub>Ce<sub>1</sub> and Pt/Al, and Ce 3d (d) of Pt/Al<sub>9</sub>Ce<sub>1</sub>.

**Table 2**  
Summary of the XPS data obtained for Pt/Al<sub>9</sub>Ce<sub>1</sub> and Pt/Al.

Catalysts	Species	Binding energy (eV)	O <sub>II</sub> /(O <sub>L</sub> +O <sub>II</sub> )
Pt/Al <sub>9</sub> Ce <sub>1</sub>	O <sub>L</sub> , O <sub>II</sub>	530.4, 532.0	74.6%
Pt/Al	O <sub>L</sub> , O <sub>II</sub>	530.5, 532.0	77.2%
Pt/Al <sub>7</sub> Ce <sub>3</sub>	O <sub>L</sub> , O <sub>II</sub>	530.3, 531.8	40.7%
Pt/Ce	O <sub>L</sub> , O <sub>II</sub>	529.1, 530.4, 531.9	23.7%
Pt/TiO <sub>2</sub>	O <sub>L</sub> , O <sub>II</sub>	529.6, 531.9	16.7%
Pt/c-Al <sub>2</sub> O <sub>3</sub>	O <sub>L</sub> , O <sub>II</sub>	530.5, 531.8	43.3%

880.9, 885.2, 899.1, 903.7 and 916.7 eV [54]. The peaks at ca. 880.9, 885.2, 899.1 and 903.7 eV are attributed to Ce(III) 3d, and those at ca. 882.6, 888.4, 898.0, 901.0, 907.4 and 916.7 eV are attributed to Ce(IV) 3d, respectively. This suggests the coexistence of Ce(III) and Ce(IV) in the Pt/Al<sub>9</sub>Ce<sub>1</sub> catalyst. The amount of Ce(III) calculated according to equation shown below [55] is ca. 72.8%:

$$\text{Ce(III)\%} = \text{Ce(III)} / (\text{Ce(III)} + \text{Ce(IV)})$$

where Ce(III) and Ce(IV) represent the respective sums of the total peak areas corresponding to the Ce(III) and Ce(IV) XPS signals. High % of Ce(III) indicates the dominance of Ce(III) state, which increases the reduction ability of Pt/Al<sub>9</sub>Ce<sub>1</sub>. It was reported that Pt can catalyze the reduction of metal oxide in the presence of NaBH<sub>4</sub> [32]. The result suggests the strong interaction of Pt and CeO<sub>2</sub> nanoparticles and thus, the weakening of the Ce—O bond in CeO<sub>2</sub>. The synergy of the metal-support interface would provide more active oxygen species, which are beneficial for HCHO oxidation reaction [56].

The H<sub>2</sub>-TPR profiles measured for Pt/Al<sub>9</sub>Ce<sub>1</sub> and Pt/Al (Fig. 5) show three reduction peaks. The first reduction peak at ca. 102–108 °C is related to the reduction of PtO<sub>x</sub> (such as Pt<sup>2+</sup>). For Pt/Al<sub>9</sub>Ce<sub>1</sub>, the second reduction peak at ca. 238 °C is attributed to

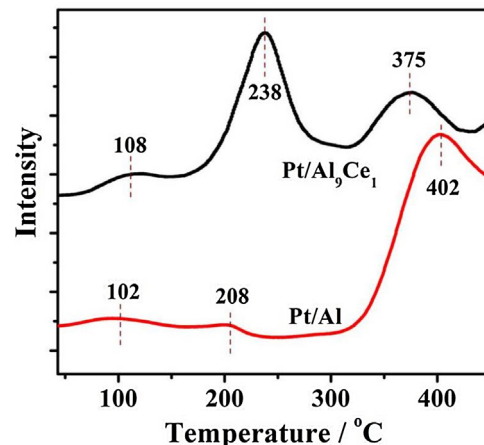


**Fig. 5.** H<sub>2</sub>-TPR profiles of Pt/Al<sub>9</sub>Ce<sub>1</sub> and Pt/Al catalysts.

the reduction of surface hydroxyl and oxygen species generated by CeO<sub>2</sub> [20,21], while for Pt/Al, the peak at ca. 208 °C is related to the reduction of surface hydroxyls. A high-temperature shift and strong intensity of the second peak for Pt/Al<sub>9</sub>Ce<sub>1</sub> are associated with the surface oxygen species, suggesting that CeO<sub>2</sub> modification can produce active oxygen species due to the oxygen storage ability of CeO<sub>2</sub>. The third peak at ca. 375 °C for Pt/Al<sub>9</sub>Ce<sub>1</sub>, while at ca. 402 °C for Pt/Al, is attributed to the reduction of lattice oxygen of the support. The low-temperature shift of the third peak for Pt/Al<sub>9</sub>Ce<sub>1</sub> implies the existence of the strong interaction between AlOOH and CeO<sub>2</sub>. This strong interaction presumably facilitates the surface capping oxygen of CeO<sub>2</sub> to capture the adsorbed HCHO

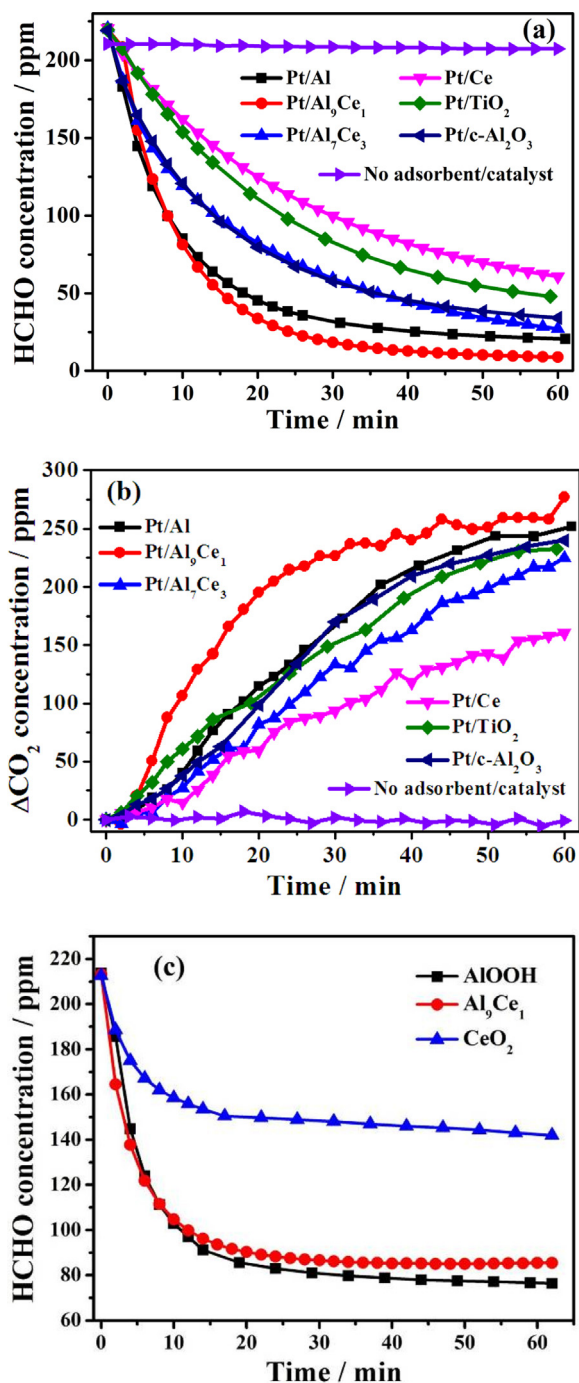


**Fig. 6.** The concentration change of formaldehyde (a) and  $\Delta\text{CO}_2$  (b) as a function of reaction time for Pt/Al, Pt/Al<sub>9</sub>Ce<sub>1</sub>, Pt/Al<sub>7</sub>Ce<sub>3</sub>, Pt/Ce, Pt/TiO<sub>2</sub> and Pt/c-Al<sub>2</sub>O<sub>3</sub> catalysts, and in the absence of the adsorbent/catalyst, (c) the decrease of HCHO concentration as a function of test time on AlOOH, Al<sub>9</sub>Ce<sub>1</sub> and CeO<sub>2</sub> adsorbents.

on the adjacent AlOOH, and subsequently to enhance the HCHO oxidation over the catalyst.

Fig. 6a and b show a comparison of the catalytic performance of the as-prepared samples. No obvious changes in  $\Delta\text{CO}_2$  and HCHO concentration are observed in the absence of the adsorbent/catalyst. The decrease in the HCHO concentration and increase in the CO<sub>2</sub> concentration, as well as no change of CO concentration (not shown), are observed as a function of reaction time for all the catalysts, implying a complete decomposition of HCHO into CO<sub>2</sub> and water at room temperature. The HCHO concentration on Pt/Al<sub>9</sub>Ce<sub>1</sub> decreases much faster than those on Pt/Al, Pt/Al<sub>7</sub>Ce<sub>3</sub>,

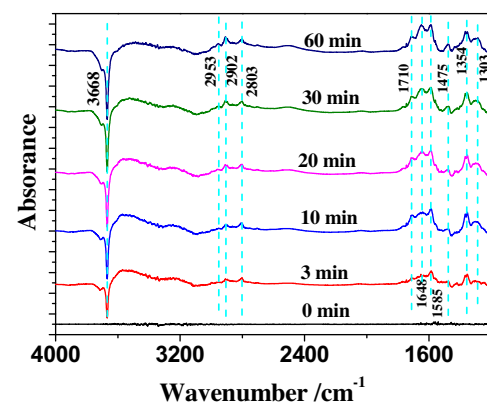


**Fig. 7.** Dynamic changes of in-situ DRIFTS on Pt/Al<sub>9</sub>Ce<sub>1</sub> catalyst as a function of time in a flow of O<sub>2</sub> + HCHO at room temperature.

Pt/TiO<sub>2</sub>, Pt/c-Al<sub>2</sub>O<sub>3</sub> and Pt/Ce. That is, the HCHO concentration after 60 min drops from ca. 230 ppm to 19.0, 30.6, 37.2, 70.7, 58.0, 44.1 ppm for Pt/Al<sub>9</sub>Ce<sub>1</sub>, Pt/Al, Pt/Al<sub>7</sub>Ce<sub>3</sub>, Pt/Ce, Pt/TiO<sub>2</sub> and Pt/c-Al<sub>2</sub>O<sub>3</sub>, respectively. Accordingly the CO<sub>2</sub> concentrations rise to ca. 277, 252, 225, 160, 233 and 240 ppm for Pt/Al<sub>9</sub>Ce<sub>1</sub>, Pt/Al, Pt/Al<sub>7</sub>Ce<sub>3</sub>, Pt/Ce, Pt/TiO<sub>2</sub> and Pt/c-Al<sub>2</sub>O<sub>3</sub>, respectively. The above results indicate that the activity of the catalysts toward oxidative decomposition of HCHO is different [57], and Pt/Al<sub>9</sub>Ce<sub>1</sub> shows higher catalytic activity than Pt/Al, Pt/Al<sub>7</sub>Ce<sub>3</sub>, Pt/Ce, Pt/TiO<sub>2</sub> and Pt/c-Al<sub>2</sub>O<sub>3</sub>. The excellent catalytic activity of Pt/Al<sub>9</sub>Ce<sub>1</sub> is mainly due to the relatively high specific surface area, abundance of surface hydroxyls, relatively good adsorption performance of the support (as shown in Fig. 6c), and oxygen storage ability of CeO<sub>2</sub>. The observed increase in the CO<sub>2</sub> concentration is larger than the decrease in the HCHO concentration, mainly due to desorption of some HCHO molecules from the reactor surface during experiment and subsequent their oxidation to CO<sub>2</sub>, as well as the measurement accuracy of CO<sub>2</sub>.

To detect the intermediates formed during the HCHO catalytic oxidation, the in-situ DFTIR spectra of Pt/Al<sub>9</sub>Ce<sub>1</sub> catalyst upon exposure to HCHO/O<sub>2</sub> at room temperature are shown in Fig. 7. The bands are visible at 3668, 2953, 2902, 2803, 1710, 1648, 1585, 1475, 1354 and 1303 cm<sup>-1</sup>, and their intensities increase with the increasing of time, and reach a steady level after ca. 30 min. The negative band at ca. 3668 cm<sup>-1</sup> can be attributed to the consumption of the surface OH groups [58,59]. The bands at 2953, 2902 and 2803 cm<sup>-1</sup> are related to  $\delta(\text{CH})$  in adsorbed HCOO,  $\nu_s(\text{CH}_2)$  and  $2\omega(\text{CH}_2)$  in dioxymethylene (DOM), respectively [60]. The bands at 1710, 1585 and 1354 cm<sup>-1</sup> are associated with  $\nu(\text{CO})$ ,  $\nu_a(\text{OCO})$  and  $\nu_s(\text{OCO})$  in adsorbed HCOO, respectively [59,60], and the bands at 1475, 1303 and 1648 cm<sup>-1</sup> are assigned to  $\delta(\text{CH}_2)$  and  $\tau(\text{CH}_2)$  in (DOM) and  $\delta(\text{H}_2\text{O})$  [60], respectively. This result indicates the formation of DOM and formate species during the HCHO catalytic oxidation process. There is no obvious peak attributed to the molecularly adsorbed HCHO on the catalyst under flowing HCHO + O<sub>2</sub> at room temperature, suggesting that the adsorbed HCHO instantly decompose into the formate species on the catalyst.

The possible mechanism for enhanced catalytic oxidation of HCHO over Pt/Al<sub>9</sub>Ce<sub>1</sub> catalyst is shown in Fig. 8. The improvement of catalytic activity for HCHO oxidation over Pt/Al<sub>9</sub>Ce<sub>1</sub> catalyst might be due to the fact that the incorporation of CeO<sub>2</sub> into AlOOH support could generate extra surface oxygen species on CeO<sub>2</sub> participating in the HCHO oxidation, which results in enhancing catalytic activity. Based on the in-situ DRIFTS spectra and previous reports [20,21,34], CeO<sub>2</sub>, due to its well-known oxygen storage capacity, could interact with the oxygen molecules in air via redox cycle of Ce<sup>4+</sup>/Ce<sup>3+</sup> and provide active oxygen species (O<sup>•</sup>). The gen-

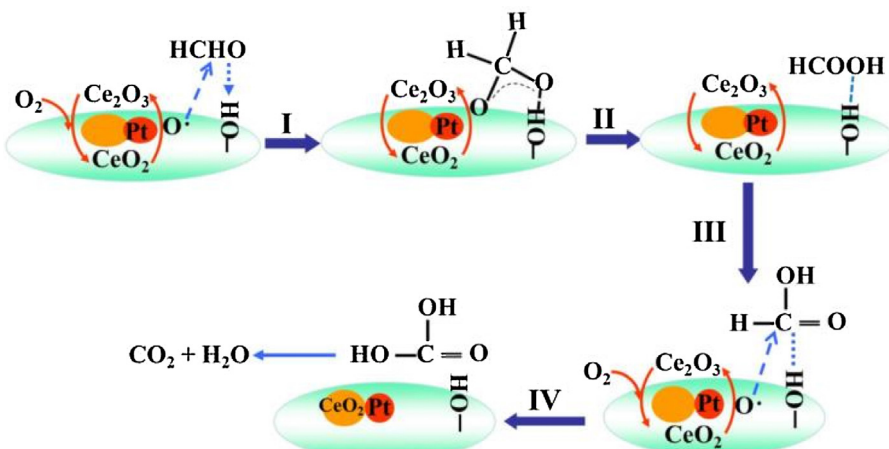


Fig. 8. Proposed mechanism for enhanced catalytic oxidation of HCHO over Pt/Al<sub>9</sub>Ce<sub>1</sub>.

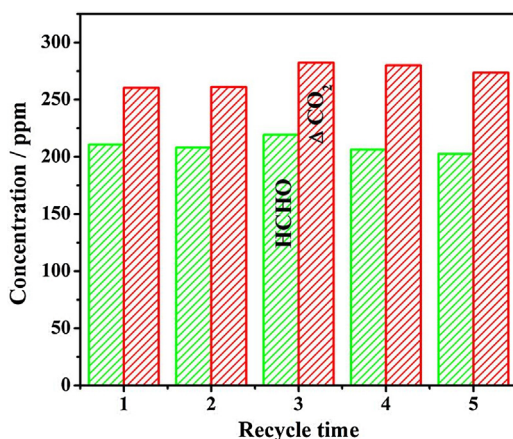


Fig. 9. Comparison of HCHO removal with recycle times over Pt/Al<sub>9</sub>Ce<sub>1</sub> catalyst. The initial concentration of HCHO is ca. 230 ppm.

erated active oxygen can attack the adjacent HCHO adsorbed on the AlOOH nanoflake via hydrogen bond. Then the HCHO molecule is oxidized to dioxymethylene (DOM) (step I), which can reconstruct into adsorbed HCOOH [(HCOOH)<sub>ads</sub>] (step II). After that, the newly formed active oxygen on CeO<sub>2</sub> further attack (HCOOH)<sub>ads</sub> (step III), and finally (HCOOH)<sub>ads</sub> completely decomposes into CO<sub>2</sub> and H<sub>2</sub>O (step IV). The aforementioned consecutive oxygen pathway presumably facilitates the oxidation of HCHO over Pt/Al<sub>9</sub>Ce<sub>1</sub> catalyst.

Fig. 9 shows the re-use of Pt/Al<sub>9</sub>Ce<sub>1</sub> catalyst at room temperature oxidation of HCHO. As can be seen the decreasing concentration of HCHO and increasing CO<sub>2</sub> concentration over Pt/Al<sub>9</sub>Ce<sub>1</sub> for five repeated cycles did not evidently change as compared to that obtained in the first-cycle, suggesting high stability of the catalyst. This result implies that Pt/Al<sub>9</sub>Ce<sub>1</sub> shows a great potential as an efficient catalyst for complete decomposition of HCHO at room temperature.

#### 4. Conclusions

Mesoporous AlOOH and CeO<sub>2</sub> nanocomposite with dispersed Pt catalyst was prepared using water-in-oil microemulsion and NaBH<sub>4</sub>-reduction processes. The resulting Pt/Al<sub>9</sub>Ce<sub>1</sub> catalyst showed an enhanced catalytic activity toward complete oxidation of gaseous HCHO at room temperature as compared to Pt/Al. Formate species are the important reaction intermediates, which can be further oxidized into CO<sub>2</sub> over the catalyst. The outstanding per-

formance of Pt/Al<sub>9</sub>Ce<sub>1</sub> for HCHO removal at room temperature is mainly attributed to the abundance of surface hydroxyls, oxygen storage ability of CeO<sub>2</sub> nanoparticles, relatively large surface area and pore volume of the catalyst. This work may potentially open an avenue for the design and fabrication of efficient catalysts for the removal of indoor HCHO pollutant at room temperature.

#### Acknowledgements

This work was supported by 973 Program (2013CB632402), the National Natural Science Foundation of China (Nos. 21307038, 21577046, 21433007, 51320105001 and 51272199), the Natural Science Foundation of Hubei Province (2015CFA001), the Fundamental Research Funds for the Central Universities (WUT: 2015-III-034) and Innovative Research Funds of SKLWUT (2015-ZD-1).

#### References

- [1] A.M. Ewlad-Ahmed, M.A. Morris, S.V. Patwardhan, L.T. Gibson, Environ. Sci. Technol. 46 (2012) 13354–13360.
- [2] J. Zhang, Y. Li, Y. Zhang, M. Chen, L. Wang, C. Zhang, H. He, Sci. Rep. 5 (2015) 12950.
- [3] Z. Xu, J. Yu, J. Low, M. Jaroniec, ACS Appl. Mater. Interfaces 6 (2014) 2111–2117.
- [4] Y. Matsuo, Y. Nishino, T. Fukutsuka, Y. Sugie, Carbon 46 (2008) 1162–1163.
- [5] Z. Xu, J. Yu, G. Liu, B. Cheng, P. Zhou, X. Li, Dalton Trans. 42 (2013) 10190–10197.
- [6] P. Fu, P. Zhang, J. Li, Appl. Catal. B: Environ. 105 (2011) 220–228.
- [7] W. Liang, J. Li, Y. Jin, Build. Environ. 51 (2012) 345–350.
- [8] P. Fu, P. Zhang, Chin. J. Catal. 35 (2014) 210–218.
- [9] C. Zhang, H. He, K. Tanaka, Catal. Commun. 6 (2005) 211–214.
- [10] C. Ma, D. Wang, W. Xue, B. Dou, H. Wang, Z. Hao, Environ. Sci. Technol. 45 (2011) 3628–3634.
- [11] J. Wang, P. Zhang, J. Li, C. Jiang, R. Yunus, J. Kim, Environ. Sci. Technol. 49 (2015) 12372–12379.
- [12] J. Yu, X. Li, Z. Xu, W. Xiao, Environ. Sci. Technol. 47 (2013) 9928–9933.
- [13] H. Huang, D.Y.C. Leung, J. Catal. 280 (2011) 60–67.
- [14] Y. Wang, A. Zhu, B. Chen, M. Crocker, C. Shi, Catal. Commun. 36 (2013) 52–57.
- [15] B. Bai, H. Arandiyani, J. Li, Appl. Catal. B 142–143 (2013) 677–683.
- [16] X. Tang, Y. Li, X. Huang, Y. Xu, H. Zhu, J. Wang, W. Shen, Appl. Catal. B 62 (2006) 265–273.
- [17] R. Spinicci, M. Faticanti, P. Marini, S. De Rossi, P. Porta, J. Mol. Catal. A 197 (2003) 147–155.
- [18] L. Qi, B. Cheng, W. Ho, G. Liu, J. Yu, ChemNanoMat 1 (2015) 58–67.
- [19] H. Huang, D.Y.C. Leung, ACS Catal. 1 (2011) 348–354.
- [20] B. Chen, X. Zhu, M. Crocker, Y. Wang, C. Shi, Appl. Catal. B 154–155 (2014) 73–81.
- [21] Q. Xu, W. Lei, X. Li, X. Qi, J. Yu, G. Liu, J. Wang, P. Zhang, Environ. Sci. Technol. 48 (2014) 9702–9708.
- [22] N. An, Q. Yu, G. Liu, S. Li, M. Jia, W. Zhang, J. Hazard. Mater. 186 (2011) 1392–1397.
- [23] C. Zhang, H. He, Catal. Today 126 (2007) 345–350.
- [24] L. Qi, B. Cheng, J. Yu, W. Ho, J. Hazard. Mater. 301 (2016) 522–530.

[25] L. Qi, W. Ho, J. Wang, P. Zhang, J. Yu, *Catal. Sci. Technol.* 5 (2015) 2366–2377.

[26] H. Huang, D.Y.C. Leung, D. Ye, *J. Mater. Chem.* 21 (2011) 9647–9652.

[27] D.Y.C. Leung, X. Fu, D. Ye, H. Huang, *Kinet. Catal.* 53 (2012) 239–246.

[28] C. Zhang, Y. Li, Y. Wang, H. He, *Environ. Sci. Technol.* 48 (2014) 5816–5822.

[29] C. Zhang, F. Liu, Y. Zhai, H. Ariga, N. Yi, Y. Liu, K. Asakura, M. Flytzani-Stephanopoulos, H. He, *Angew. Chem. Int. Ed.* 51 (2012) 9628–9632.

[30] B.B. Chen, C. Shi, M. Crocker, Y. Wang, A.M. Zhu, *Appl. Catal. B* 132–133 (2013) 245–255.

[31] B.B. Chen, X. Zhu, M. Crocker, Y. Wang, C. Shi, *Catal. Commun.* 42 (2013) 93–97.

[32] Z. Yan, Z. Xu, J. Yu, M. Jaroniec, *Environ. Sci. Technol.* 49 (2015) 6637–6644.

[33] N. An, W. Zhang, X. Yuan, B. Pan, G. Liu, M. Jia, W. Yan, W. Zhang, *Chem. Eng. J.* 215–216 (2013) 1–6.

[34] Z. Xu, J. Yu, M. Jaroniec, *Appl. Catal. B* 163 (2015) 306–312.

[35] C. Kim, L. Thompson, *J. Catal.* 244 (2006) 248–250.

[36] J.A. Rodriguez, S. Ma, P. Liu, J. Hrbek, J. Evans, M. Perez, *Science* 318 (2007) 1757–1760.

[37] X. Liang, J. Xiao, B. Chen, Y. Li, *Inorg. Chem.* 49 (2010) 8188–8190.

[38] Y. Lee, G. He, A.J. Akey, R. Si, M. Flytzani-Stephanopoulos, I.P. Herman, *J. Am. Chem. Soc.* 133 (2011) 12952–12955.

[39] N. Yi, R. Si, H. Saltsburg, M. Flytzani-Stephanopoulos, *Energy Environ. Sci.* 3 (2010) 831–837.

[40] N. Pal, E. Cho, D. Kim, M. Jaroniec, *J. Phys. Chem. C* 118 (2014) 15892–15901.

[41] Y. Shen, X. Yang, Y. Wang, Y. Zhang, H. Zhu, L. Gao, M. Jia, *Appl. Catal. B* 79 (2008) 142–148.

[42] Z. Xu, J. Yu, W. Xiao, *J. Chem. Eur.* 19 (2013) 9592–9598.

[43] S.H. Joo, J.Y. Park, C.K. Tsung, Y. Yamada, P. Yang, G.A. Somorjai, *Nat. Mater.* 8 (2009) 126–131.

[44] Z. Xu, J. Yu, G. Liu, *Electrochim. Commun.* 13 (2011) 1260–1263.

[45] R. Raza, Q. Liu, J. Nisar, X. Wang, Y. Ma, B. Zhu, *Electrochim. Commun.* 13 (2011) 917–920.

[46] T. Montini, M. Melchionna, M. Monai, P. Fornasiero, *Chem. Rev.* (2016), <http://dx.doi.org/10.1021/acs.chemrev.5b00603>.

[47] L. Nie, J. Yu, X. Li, B. Cheng, G. Liu, M. Jaroniec, *Environ. Sci. Technol.* 47 (2013) 2777–2783.

[48] A. Altamirano-Gutiérrez, A.M. Fernández, F.J. Rodríguez Varela, *Int. J. Hydrogen Energy* 38 (2013) 12657–12666.

[49] G. He, Y. Song, K. Liu, A. Walter, S. Chen, S. Chen, *ACS Catal.* 3 (2013) 831–838.

[50] C. Sangwichien, G.L. Aranovich, M.D. Donohue, *Colloids Surf. A* 206 (2002) 313–320.

[51] H. Huang, P. Hu, H. Huang, J. Chen, X. Ye, D.Y.C. Leung, *Chem. Eng. J.* 252 (2014) 320–326.

[52] L. Nie, A. Meng, J. Yu, M. Jaroniec, *Sci. Rep.* 3 (2013) 3215.

[53] J.D. Tannenbaum, *Chem. Mater.* 18 (2006) 4793–4801.

[54] E. Bêche, P. Charvin, D. Perarnau, S. Abanades, G. Flamant, *Surf. Interface Anal.* 40 (2008) 264–267.

[55] D.R. Mullins, S.H. Overbury, D.R. Huntley, *Surf. Sci.* 409 (1998) 307–319.

[56] H.F. Li, N. Zhang, P. Chen, M.F. Luo, J.Q. Lu, *Appl. Catal. B* 110 (2011) 279–285.

[57] X. Ke, X. Zhang, J. Zhao, S. Sarina, J. Barry, H. Zhu, *Green Chem.* 15 (2013) 236–244.

[58] J. Araña, C. Garriga i. Cabo, J.M. Doña-Rodríguez, O. González-Díaz, J.A. Herrera-Melíán, J. Pérez-Peña, *Appl. Surf. Sci.* 239 (2004) 60–71.

[59] J. Raskó, T. Kecske, J. Kiss, *J. Catal.* 224 (2004) 261–268.

[60] T. Kecske, J. Raskó, J. Kiss, *Appl. Catal. A* 273 (2004) 55–62.